Journal of the European Ceramic Society 46 (2026) 118684

Contents lists available at ScienceDirect

Journal of the European Ceramic Society

journal homepage: www.elsevier.com/locate/jeurceramsoc

Macroscopic strength and failure of dislocation-engineered MgO

Maximilian Staudacher [a,*], Oliver Preuß [b,1], Xufei Fang [b], Tanja Lube [a]

[a] Department of Materials Science, Chair of Structural and Functional Ceramics, Montanuniversität Leoben, Franz Josef-Straße 18, Leoben 8700, Austria
[b] Institute for Applied Materials, Karlsruhe Institute of Technology, Kaiserstraße 12, Karlsruhe 76131, Germany

ARTICLE INFO

Keywords:
Fractography
Dislocations
Failure Analysis
MgO
Finite Element Analysis

ABSTRACT

Dislocations in ceramics can enhance mechanical performance and functional properties. Recently, tailoring the dislocation density in ceramics at meso/macroscale at room temperature was made available through a surface scratching technique. The effects of this treatment on the material's hardness, crack-initiation/propagation and microscopic strength were investigated, with an observed toughening effect. Here we investigated the impact of dislocation density, tuned via surface scratching technique, on the macroscopic strength of MgO crystals. Specimens with three different dislocation densities were tested: unaltered as-received state ($<10^{12}$ m^{-2}), an intermediate density ($\sim10^{14}$ m^{-2}), and a high density ($>10^{15}$ m^{-2}). The macroscopic strength was assessed using Ball-on-Three-Balls-tests and Ball-on-Ring-tests. The influence of anisotropic material properties on the stress field and the susceptibility to specimen edge failures was assessed through Finite Element Analysis. Extensive fractographic analysis suggests the observed decrease in the macroscopic strength can be related to the creation of local stress concentrations during dislocation engineering.

1. Introduction

Oxide ceramic materials are widely valued as structural materials for their high melting points, chemical stability and exceptional stiffness, yet their macroscopic mechanical performance is fundamentally limited by their brittle nature [1,2]. Unlike most engineering-relevant metals, where plastic deformation can dissipate the energy and delay catastrophic failure, most ceramics exhibit minimal dislocation activity at ambient conditions due to very limited dislocation activities, a consequence of low dislocation densities (typically $\sim10^{10}$ m^{-2}), high bond strength, large Burgers vectors, and complex crystal structures. As a result, fracture in ceramics occurs with little warning, and their strength is typically governed by the size and distribution of flaws. The utilization of high dislocation densities could give a unique way out of this conjuncture [3].

Early investigations into dislocation activity in ionic crystals during the 1950s and 1960s focused primarily on rock-salt–structured materials such as NaCl [4], LiF [5,6], and MgO [7]. These studies revealed that especially at elevated temperatures, these oxides and halides exhibit substantial ductility (>10% strain) [8,9], enabled by highly mobile dislocations that can multiply readily under applied load. At room temperature, however, plasticity is often far more limited, though still measurable [7]. The prevailing explanation lies in the extremely low pristine dislocation densities characteristic of these materials: with so few mobile defects available, the onset of macroscopic plastic deformation is hindered. The dislocation activity of oxides is highly sensitive to the choice of material [10]. MgO, which was used extensively in the early foundational studies, stands out as an ideal model system for probing how dislocations can influence the strength and fracture behavior of ceramics [11].

Recently, mesoscopic plastic deformation by the use of cyclic Brinell indentation [12] and cyclic Brinell ball scratching [13] have made it possible to introduce and control dislocation densities in suitable ceramics up to $\sim10^{15}$ m^{-2}, a 10,000-fold increase in comparison to pristine crystals. These capabilities reopen fundamental questions about the mechanical role of dislocations in materials that are traditionally classified as brittle, since the sluggish natural dislocation multiplication can be deliberately pre-empted. Increasing the dislocation density prior to mechanical testing enables systematic exploration of how their interaction with pre-existing flaws affect failure initiation, strength statistics, and fracture resistance at the macroscale.

Zones of high dislocation densities are expected to influence strength

* Corresponding author.
E-mail address: maximilian.staudacher@unileoben.ac.at (M. Staudacher).
[1] Previously at: Division Nonmetallic-Inorganic Materials, Department of Materials and Earth Sciences, Technical University of Darmstadt, Peter-Grünberg-Straße 2, 64287 Darmstadt, Germany.

https://doi.org/10.1016/j.jeurceramsoc.2026.118684
Received 3 February 2026; Received in revised form 10 July 2026; Accepted 13 July 2026
Available online 13 July 2026

in several competing ways. On one hand, dislocations can generate significant lateral compressive residual stresses (in the GPa-range), which may offset tensile loads and retard crack initiation [14,15]. Pile-ups of dislocations, e.g. caused by the Lomer lock mechanism, could simultaneously promote fracture by creating strong localized driving forces [16,17]. On the other hand, the presence of distributed dislocations can alter crack propagation behavior once the crack is initiated. Typical toughening mechanisms based on crack tip-dislocation interaction include shielding effects by the stress fields around dislocations lowering the local stress intensity factor [18], the emission of (shielding) dislocations from the crack tip [19,20], and the blunting of the crack tip in case the glide planes are inclined to the fracture plane [21]. Furthermore, a high density of engineered defects can modify the statistical nature of fracture. According to the statistical theory of strength, the scatter in strength measurements is governed by the distribution of critical flaws [22,23]. Modifying the defect density in a controlled manner could effectively homogenize the flaw landscape, potentially increasing the Weibull modulus and reducing strength variability.

With mechanisms potentially both increasing and decreasing the resistance against crack initiation and propagation, the influence of a deliberately increased pre-existing dislocation density on the macroscopic strength of oxides is still unclear and will be the major focus of this work. More specifically, this work will present results of a case study using single-crystal MgO. On the micro- and mesoscale, the influence of dislocation-rich zones on the fracture behavior of MgO has already been investigated and discussed recently using Vickers indentation [24] and the double cleavage drilled compression test [25]. To probe the macroscopic effect, two consecutive trials were carried out, with the result of the first trial defining the design of the second. Therefore, the results of each trial will be presented and discussed separately.

Additionally, the challenges of strength testing of stiff, brittle materials which are prone to plastic deformation shall be pointed out. The observations from this work will be used to derive the special requirements for the utilized methods, which were originally developed without considering plasticity. Thus, testing guidelines to ensure accurate and reliable strength assessment are presented. These findings will not only be relevant for MgO, but for plenty of other plastically deformable ceramics as well [10].

2. Experimental

2.1. Material and specimen preparation

Undoped MgO single crystals were sourced from Alineason Materials Technology GmbH (Frankfurt am Main, Germany) in two batches. For both batches, specimens were delivered as square plates in a single-side polished condition. The crystal orientation within each specimen was chosen so that the specimen faces were parallel to {100} planes and that the specimen edges were parallel to ⟨100⟩ directions. Batch 1 consisted of a total of 40 specimens, while batch 2 comprised 30 specimens. The dimensions and further specimen information are given in Table 1.

To increase the dislocation density, the Brinell ball scratching technique, as outlined in [13], was utilized. This technique allows to tailor the surface-near dislocation density at room temperature by repeatedly scratching a hard sphere over the sample with a controlled normal load. Brinell scratching relies on the activation of pre-existing dislocation sources in the material, which should be abundant because of the pristine dislocation density already present in the sample (roughly 7×10^{11} m^{-2}). The dislocation density can be estimated by electron channelling contrast imaging (ECCI), which allows the visualization of individual dislocations in a scanning electron microscope (here MIRA3-XM, Tescan, Brno, Czech Republic) [26]. The density is obtained by counting the dislocations per area (for more detailed analysis on similar samples, refer to e.g. [24]).

The scratching was realized on a “Finotest” universal hardness tester (Karl Frank GmbH, 69488 Weinheim-Birkenau, Germany) equipped with a two-axis stage (Thorlabs Inc., Newton NJ 07860, USA). Scratching was performed using a hardened-steel ball of 2.5 mm diameter with a load of 9.81 N (1 kgf) and a scratching speed of 0.5 mm/s. With this method, the dislocation density on the surface as well as within the underlying bulk (up to a depth of about 200 μm) can be tailored by the number of passes per wear track. Specimens were scratched in parallel lines (150 μm distance from center to center, to match the width of the wear tracks) within a square region (3 mm × 3 mm for batch 1, 6 mm × 6 mm for batch 2) in the center of the polished surface at room temperature. A representative example from batch 1 is illustrated in Fig. 1, with scratching tracks visible as vertical lines in the specimen’s center. High-resolution SEM analysis confirmed that no cracks were present after scratching.

For batch 1, specimens were randomly grouped into two samples before scratching. One sample represents reference specimens (designated as sample B3B−0), which were not altered in any way, and the other represents specimens with a greatly increased dislocation density (designated as sample B3B−10), which were scratched with 10 passes. For batch 2, specimens were randomly grouped into three samples before scratching. This time, reference specimens (designated as sample BoR−0), specimens with a moderately increased dislocation density

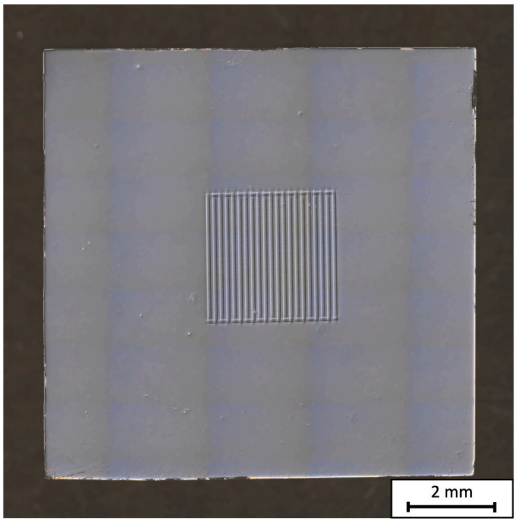

Fig. 1. A representative specimen of batch 1 with the dislocation engineered region visible as vertical lines in the center of the specimen on the polished face. The lines are made visible by using differential inference contrast in a light microscope.

Table 1
Information on the sample designation, average specimen dimensions with respective standard deviation, approximate dislocation densities and sample size.

Designation [-]	Batch [-]	Edge length [mm]	Thickness [mm]	No. of Scratches [-]	Dislocation density [m^{-2}]	Sample size [-]
B3B−0	1	9.956 ± 0.068	0.553 ± 0.011	None	~$7{\cdot}10^{11}$	20
B3B−10	1	9.975 ± 0.092	0.549 ± 0.013	10	~$2{\cdot}10^{15}$	19
BoR−0	2	24.996 ± 0.110	0.541 ± 0.009	None	~$7{\cdot}10^{11}$	10
BoR−1	2	25.034 ± 0.081	0.532 ± 0.012	1	~$4{\cdot}10^{14}$	10
BoR−10	2	25.051 ± 0.086	0.528 ± 0.021	10	~$2{\cdot}10^{15}$	10

(designated as sample BoR−1) and specimens with a greatly increased dislocation density (designated as sample BoR−10) were produced. For samples BoR−1 and BoR−10, the dislocation density was increased through a single and through 10 passes, respectively. The dislocation densities for all samples are identical to those determined in [24].

No additional steps that might alter the surface quality or defect distribution of the specimens were performed. Specimen edge chamfering was deemed not feasible (at least without damage) due to the low specimen thickness, large edge length and low fracture toughness. Specimen edge length was measured on at least two edges per specimen with a Mitutoyo Absolute Digimatic Micrometer (Mitutoyo Corporation, Kawasaki, 213–8533, Kanagawa, Japan). Average specimen thickness was determined with a Mitutoyo Absolute Digimatic Indicator ID-C from measurements near the corners of each specimen. Prior to testing, adhesive tape was attached to the unpolished specimen side (which is loaded in compression) to aid fractography after failure. Care was taken to omit the region of load introduction to ensure a defined contact of the loading member of the test jig to the specimen without soft intermediate layers [27]. On the same side, specimens were marked with a pen line parallel to one edge and, if applicable, parallel to the scratch tracks to aid specimen alignment and fractography.

2.2. Strength testing and fractography

Strength testing was performed on a Zwick Z010 (ZwickRoell GmbH & Co. KG, 89079 Ulm, Germany) equipped with a load cell by ZwickRoell (maximum load 10 kN) operated through controllers by Doli Elektronik GmbH (72525 Münsingen, Germany). The polished specimen face was loaded in tension for all specimens.

Specimens of batch 1 were tested with the Ball-on-Three-Balls (B3B) test [28–31]. The load ball and supporting balls are made of silicon nitride with a diameter of 7.144 mm. This gives a support diameter of 8.249 mm. Due to the three-fold symmetry of the stress field, special care was taken to invariably align the specimen to the three supporting balls. All tests of batch 1 were conducted at approximately 24 °C and a relative humidity of approximately 50 %, with a constant crosshead speed of 0.5 mm/s, which lead to times to failure of approximately 7 s. Specimens of batch 2 were tested with the Ball-on-Ring (BoR) test [31–33]. The support ring diameter was 17 mm, and the loading ball diameter was 19 mm. Both were made from steel. Due to the axisymmetric stress field, invariable specimen alignment to the fixture would theoretically not have been necessary, but was still implemented. All tests of batch 2 were conducted at approximately 23 °C and a relative humidity of approximately 30 %, with a constant crosshead speed of 2 mm/s, leading to failure within 10 s. For both strength testing methods, regular stress evaluation [30,34], which are valid for isotropic materials, could not be utilized due to the anisotropic material properties of MgO single crystals. Instead, Finite Element Analysis (FEA) had to be utilized (see Section 2.3). For the B3B-tests, corrections for non-linear effects were utilized as well.

Fractographic analysis was conducted with a SZH10 stereomicroscope (Olympus K.K., 163–0914 Tokyo, Japan) and with a Leica S9i stereomicroscope (Leica Camera AG, 35578 Wetzlar, Germany). Images of fracture surfaces were captured with a BX−50 light microscope by Olympus K.K. Weibull analysis was performed according to [35]. Data analysis was conducted with Mathematica 14.0 (Wolfram Research Inc., Champaign IL 61820–7237, USA).

2.3. Finite element analysis models

In order to assess the stress field during the B3B- and BoR-test for anisotropic specimens, Finite Element Analysis was utilized. For both strength testing methods, a model was implemented in ANSYS R23.2 (ANSYS Inc., Canonsburg PA 15317, USA) through a script written in Ansys-Parametric-Design-Language (APDL). A mesh convergence analysis was performed for both models to ensure a sufficiently small element size. Linear elastic material behavior was assumed, and the elastic constants for the cubic MgO are given through c_{11} = 298.960 GPa, c_{12} = 96.420 GPa and c_{44} = 157.130 GPa [36]. For the given geometries, an ideal edge length of 10 mm and 25 mm, respectively, was assumed. To consider variable specimen thicknesses, parametric FEA results over the observed range of thickness values were generated and interpolated.

The model representing the B3B-test is depicted in Fig. 2a). The load introduction was realized through a punctiform load in the center of the plate. The plate's displacement is constrained through punctiform nodal boundary conditions representing the support balls. The model was meshed with 241220 SOLID186 elements (20 node hexahedral elements) and 1011954 nodes. The resulting stress field is shown in Fig. 3 (left). The maximum tensile stress is found on the surface in the center of the plate and is 6.40 MPa for an ideal thickness of 0.55 mm and a load of 1 N. To ease comparison between stress field characteristics, the maximum tensile stress will be normalized to the applied load from this point on, i.e. 6.40 MPa/N.

The model representing the BoR-test is shown in Fig. 2b). Again, the load introduction was realized through a punctiform load in the center of the plate. The plate's displacement is constrained through a chain of punctiform nodal boundary conditions representing the support ring. The model was meshed with 38080 SOLID186 elements and 169685 nodes. The resulting stress field is shown in Fig. 3 (right). The maximum tensile stress is found on the surface in the center of the plate and is 7.62 MPa/N for an ideal thickness of 0.55 mm. Note the distortion of the usually axisymmetric stress field (in the case of isotropic materials) due to the material's anisotropy.

While both models include the crystal's anisotropy, there are other effects that are not taken into account. First, the boundary conditions represent an idealized case, where the finite contact area between fixture and specimen is not considered. It has been shown that an increase in contact area between the loading ball and the specimen decreases the maximum tensile stress in the plate [30]. Additionally, single crystal MgO is prone to plastic deformation in Hertzian contact situations, which is also not considered with a linear elastic material model. Thus, the maximum tensile stress determined for each strength testing method is slightly underestimated. However, a qualitative analysis of the stress field itself and the differences in strength between different samples is still valid, as fracture loads are reasonably similar for all samples.

Note that a model reduction due to symmetry conditions was not considered for these models, as the underlying code is built for any crystal symmetry in any orientation, and thus overall testing symmetry is usually not given. However, in the specific cases discussed in this work, the B3B-model could have been reduced to a half-model and the BoR-model could have been reduced to a quarter-model.

3. Results and discussions

As briefly mentioned in the introduction, two trials were carried out. The results of batch 1, which were obtained with the Ball-on-Three-Balls (B3B) test, were essential for the design and success of the second trial, conducted with the Ball-on-Ring (BoR) test. Thus, each trial will be presented and discussed separately, starting with batch 1 in the following sections.

The initial choice to utilize the B3B-test was based on the following considerations. First, a very localized stress field with the maximum tensile stress located in the center of the dislocation-engineered region was necessary. Second, the B3B-test is well researched in terms of geometric and contact non-linearities [30], which were expected to occur with these specimens. Third, FEA-code for such a loading setup (which is crucial due to crystal anisotropy) was readily available and has been validated/developed over the past two decades [28–30,37].

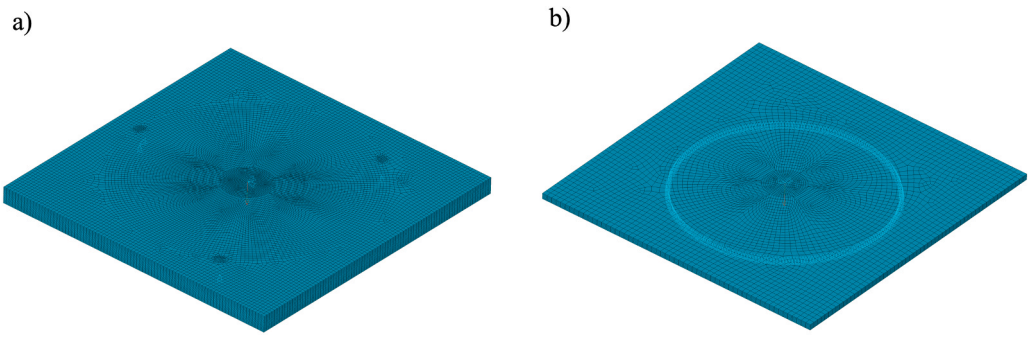

Fig. 2. FEA models utilized in this work. The model for the B3B-test is shown in a), and the model for the BoR-test in b).

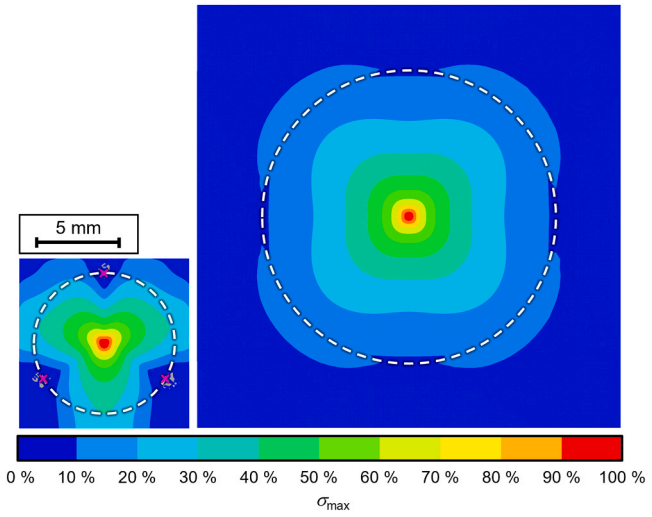

Fig. 3. Stress fields for B3B specimens (left) and for BoR specimens (right). The colors indicate the magnitude of tensile stress in 10 % percentiles, with blue as the regions with lowest (0 % −10 %) and red as the regions with highest (90 % - 100 %) stress. Gray regions indicate compressive stresses. Ball positions for the B3B-test are marked with pink crosses, and the support radius is given in white for both testing setups.

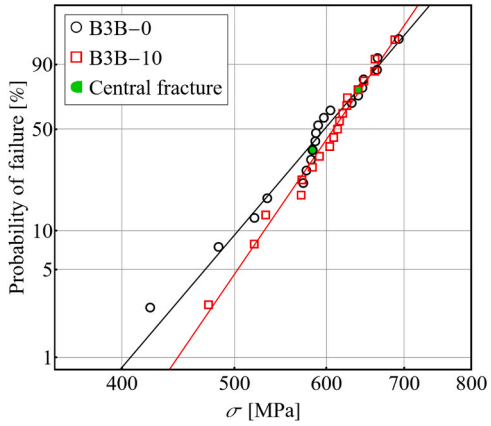

Fig. 4. Weibull diagram for samples of batch 1. Specimens that fractured in the center are marked with a green filling.

3.1. Batch 1: Ball-on-Three-Balls (B3B) testing

3.1.1. Results

The results of Weibull analysis for samples B3B−0 and B3B−10 are given in Table 2 and are shown in Fig. 4.

For both samples, the confidence intervals overlap, thus no significant difference in strength or Weibull modulus is observed. This is also confirmed by Fig. 4, where strength results in the Weibull diagram overlap and no noteworthy outliers are present.

Fractography was conducted on all specimens to analyze fracture patterns and to identify the positions of fracture origins. As shown in Fig. 5a) and b), specimens fractured along {100}-type cleavage planes, which are orthogonal to each other. With increased failure loads, an increase in the number of fragments was observed. In most cases, the primary fracture runs parallel to an edge and to a straight line connecting two of the supporting balls, i.e. along [010] as displayed in Fig. 5a) and b).

For both reference and dislocation-engineered samples, the majority of fracture origins (19 out of 20 specimens for B3B−0, 18 out of 19 specimens for B3B−10) were found to be located at the edge of the specimen, as depicted in Fig. 6a). For each sample, only a single specimen fractured in the center, as shown in Fig. 6b). The data corresponding to these specimens are also marked (in green) in Fig. 4, and both display moderate strength within the observed range of strength values.

Table 2
Results of statistical analysis of batch 1: Average fracture load P and average strength σ_{mean} with their respective standard deviation, characteristic strength σ_0, unbiased Weibull modulus m_{ub}, with 90% confidence intervals in square brackets.

Sample [-]	P [N]	σ_{mean} [MPa]	σ_0 [MPa]	m_{ub} [-]
B3B−0	97 ± 11	591 ± 65	618 [596−641]	11.0 [8.1 – 15.0]
B3B−10	97 ± 8.6	603 ± 52	625 [606−644]	13.7 [10.0 – 18.7]

3.1.2. Discussion

Fracture analysis was crucial to explain the lack of difference between the strength and Weibull modulus of the reference and scratched samples. Most specimens fractured from edge flaws, and not from the scratched region with an increased dislocation density in the specimen's center. Since the edges are of the same surface quality in both samples, no difference is expected for such a failure mode. Through FEA, the maximum stress in the center was determined to be 6.40 MPa/N. For typical positions of failure, as highlighted in Fig. 5a), a tensile stress in the range of 1.41 MPa/N to 1.58 MPa/N acts at the specimen edge. While this is only 25% of the maximum tensile stress in the center, specimen edges were of much worse quality than expected and edge failure ensued.

Additionally, a deviation from linear elastic behavior during loading was observed, as displayed in Fig. 7. To discern between the non-linearities of the overall testing setup (since only the crosshead displacement was measured) and the non-linearities that can be attributed to the material, the load-displacement curves of specimens with linear-elastic behavior were recorded as well. These specimens were made from heat treated high-speed-steel (HSS-DMO−5) in the exact

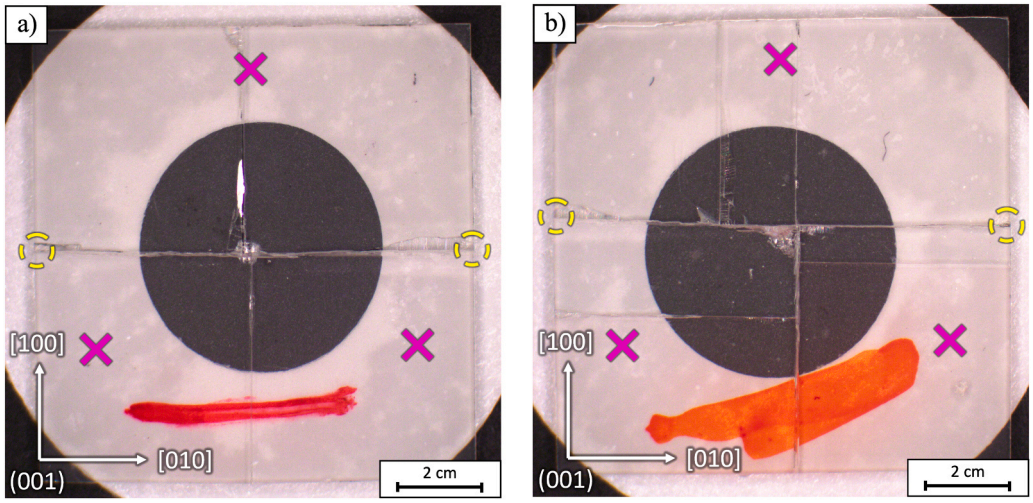

Fig. 5. Macroscopic fracture pattern of specimens from sample B3B−0. A low load fracture is given in a), and a high-load fracture is shown in b). The white ring is an adhesive tape, and the red marking helps with specimen alignment to the three supporting balls. Both aids were applied prior to testing and to the compression loaded face. Ball positions are marked with pink crosses. Typical positions of failure origins (edge failures) are marked with yellow circles.

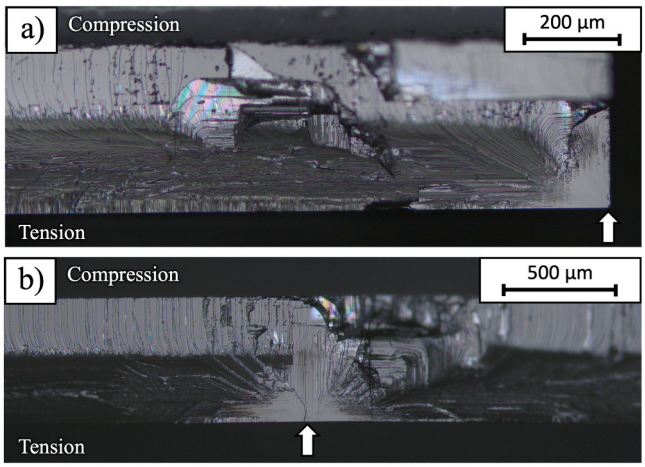

Fig. 6. Fracture surface of a specimen of sample B3B−0 with an edge failure in a) and a central fracture origin in b). Fracture origins are marked through the white arrows.

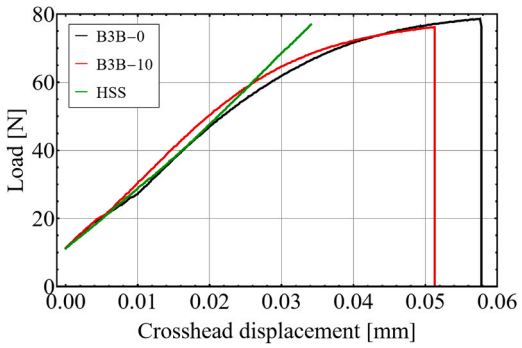

Fig. 7. Load-displacement curve for two B3B-specimens, with the black line representing a reference specimen (from sample B3B−0) and the red line representing a dislocation-engineered specimen (from sample B3B−10). The green line represents the specimen made from HSS. Note that the displacement is obtained through the crosshead displacement.

same geometries as the MgO-specimens and tested with the same testing parameters. HSS was chosen due to its similarity in Young's modulus to MgO (as can be seen from the initial section of the loading curve) and high yield strength. The load-displacement curves of MgO show a significant decrease in slope (nearly plateauing), which can be attributed to plastic deformation of the specimen in the highly stressed regions (in the regions of ball contact or in the region of maximum tensile stress). Still, the fracture itself was clearly brittle and showed no signs of ductile failure.

In order to properly assess the influence of an increased dislocation density on the measured strength, it is crucial that edge failure is avoided and that plastic deformation in contacting regions with the fixture is minimized. While an increase in edge strength would be one option, the specimen fabrication process is not in the authors' control. Thus, the testing procedure needs to be reworked to ensure failure from the dislocation-engineered regions in the center of the specimen.

3.2. Batch 2: Ball-on-Ring testing

To address the issues encountered in batch 1, the strength testing procedure was adapted for batch 2. To decrease plastic deformation in the contacting region of the loading ball and the specimen, the material and diameter of the ball were adapted. Instead of silicon nitride, a less stiff steel ball was utilized. This decreased the maximum tensile stress (according to Hertzian contact theory [38]) by 10% for a load of 100 N. By increasing the ball diameter from 7.1 mm to 19 mm, contact stresses were reduced by another 48% for a load of 100 N. To decrease plastic deformation in the contacting regions of the support balls to the specimen, a ring with a diameter of 17 mm was utilized instead. Through this shift to a Ball-on-Ring configuration, the contact area to the specimen was increased and contact stresses were reduced by 71% for a load of 100 N (again, determined through Hertzian contact theory [38]). Most importantly, to decrease the risk of edge failure, the specimen geometry was adapted. The edge length was increased from 10 mm to 25 mm, without any change in specimen thickness. Through these measures, the maximum tensile stress in the center of the specimen was raised from 6.40 MPa/N to 7.62 MPa/N, and the maximum tensile stress at the specimen edges was decreased from 1.58 MPa/N to 0.65 MPa/N. Compared to the previous testing setup (a maximum edge stress of about 25% of the maximum tensile stress), the edge stresses were significantly reduced, to about 8.6% of the maximum tensile stress. Through the increased leverage (and thus increased maximum tensile stress per applied load) compared to the previous setup, lower absolute loads are necessary to achieve a certain stress level, which also counteracts plastic

deformation.

3.2.1. Results

The results of statistical analysis for the samples BoR−0, BoR−1 and BoR−10 are given in Table 3 and are shown in Fig. 8. Due to the smaller sample size, average values instead of Weibull parameters are given. Overall, a decrease in strength from BoR−0 (reference sample) to BoR−1 (single scratch pass) to BoR−10 (ten scratch passes) is observed.

To better understand these results, fractography was performed through optical light microscopy for all specimens to discern fracture patterns and positions of fracture origin. SEM analysis of fracture surfaces was conducted as well, but yielded little additional information in the context of this work. Additionally, cleaning the specimens proved to be exceptionally difficult due to the delicacy of the specimens and subsequent surface contamination.

Again, specimens fractured along cleavage planes, as shown in Fig. 9a), b) and c), but high strength specimens also showed fractures at approximately 45° to the orthogonal fractures, as shown in in Fig. 9a) and b). In general, a significant increase in the number of fragments compared to batch 1 was observed. Similar to batch 1, primary fracture was found to be parallel to one of the specimen's edges, i.e. along the major cleavage planes. However, no preference for horizontal or vertical orientations of the primary crack in relation to the scratch tracks (see black markings in Fig. 9) was observed.

Instead of a categorization into central fracture and edge fracture, as applied for the results of batch 1, a more detailed breakdown was utilized for batch 2. No edge failures could be determined, but additional categories for central fracture were necessary instead. Several specimens exhibited a fracture origin on the compression loaded side (see Fig. 10a)), indicating failure due to contact stresses in the region of load introduction. A few specimens featured fracture origins within the bulk instead of the tensile surface, as shown in Fig. 10b). These specimens are categorized as "contact failure" and "bulk failure", respectively.

Additionally, a distinction for surface failures of specimens with scratch tracks is introduced. Specimens with the primary crack parallel to the scratch tracks were categorized into the group "parallel failure" (see Fig. 11a)), whereas specimens with a primary crack orthogonal to the scratch tracks were grouped as "orthogonal failure" (see Fig. 11b)). These failure types can be clearly distinguished on the fracture surfaces: note the unbroken line and well-defined area just beneath the tensile surface of Fig. 11a) and c), which is parallel to the scratch tracks, and the wavy structure beneath the tensile surface of Fig. 11b) and d), which represents a cross section of the scratch tracks.

In addition to the aforementioned categories, the fracture origin of some specimens could not be explicitly determined, which were thus grouped as "unknown". The application of this categorization is summarized in Fig. 12 where the strength of all specimens in samples BoR−0, BoR−1 and BoR−10 is plotted.

3.2.2. Discussion

The application of this categorization allows for identifying the outliers and conducting a censored evaluation. In the context of this work, only failures from the tensile surface in a region with an increased dislocation density are relevant. Therefore, contact failure and bulk failure are not relevant for this investigation, and the respective results can be disregarded for the censored analysis. Similarly, if the fracture origin cannot be determined, results are also not taken into account.

Table 3
Results of statistical analysis of batch 2: Average fracture load P and average strength σ_{mean} with their respective standard deviation.

Sample [-]	P [N]	σ_{mean} [MPa]
BoR−0	131 ± 22	1037 ± 204
BoR−1	112 ± 30	920 ± 252
BoR−10	94 ± 14	783 ± 159

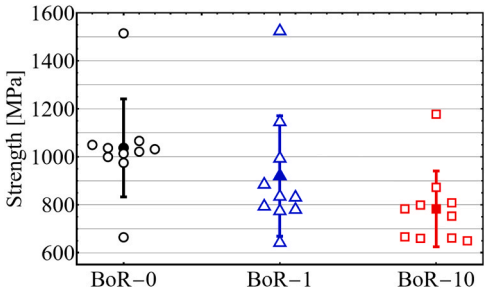

Fig. 8. Average specimen strength (filled markers) of all samples of batch 2 and respective individual values (open markers).

Thus, only the groups "surface failure", "parallel failure" and "orthogonal failure" from Fig. 12 are considered. The average strength of the remaining specimens after censoring along the unaltered average strength is given in Table 4 and plotted in Fig. 13. The larger scatter of strength values was expected and is well documented in literature [39–43].

Apart from sample BoR−1, the standard deviation generally decreased through censoring. In addition, an increase in dislocation density led to an increase of surface failures. In BoR−0, only 4 surface failures were observed, while 8 specimens failed from the surface in BoR−10. Furthermore, most of the failures in BoR−10 occurred orthogonally to the scratch tracks, while the majority of surface failures in BoR−1 were parallel to the scratch tracks.

Again, a deviation from linear elastic behavior during loading was observed, as evident from Fig. 14a). As with batch 1, a comparison to a specimen made from HSS (same dimensions as the MgO specimens in batch 2) clearly shows the non-linearity of the material. To aid a comparison of batch 1 and batch 2, Fig. 14b) shows the load over the normalized displacement. For batch 2, the load-displacement curves show a significant decrease in slope only in the low-load regions, with a linear elastic behavior once 20% of the final displacement has been passed. This indicates an absence of plastic deformation during testing after an initial deformation stage. Thus, rough estimates of the maximum shear stresses caused by contact stresses of the loading ball were determined. According to linear elastic Hertzian contact theory [38], a maximum shear stress of 570 MPa during BoR-testing, 1030 MPa during B3B-testing and 870 MPa during scratching is acting beneath the relevant contacting sphere. While this is an oversimplification of the stress field and the mechanisms involved, it helps to put the observed results into perspective. For batch 1, shear stresses during loading exceed those acting during scratching, so plastic deformation occurs beneath the loading ball, which results in a flattening of the load displacement curves. For batch 2, even for the maximum load, shear stresses are well below the threshold used in scratching, and specimens would thus encounter little plastic deformation beneath the loading ball. Ultimately, this results in linearly increasing load displacement curves.

4. Deductions

4.1. Impact of dislocations on strength

In comparison to previous studies, which reported an increase in hardness, damage tolerance [24] and crack resistance [25] with increased dislocation density in mesoscale tests, the observed decrease in macroscopic strength is unexpected.

This is most likely due to damage and residual stresses that are introduced during the scratching process. Considering the measured strength values and a K_{Ic} of 0.8–1.8 $MPa\sqrt{m}$ [44–46], a critical crack size of 0.5 µm – 3 µm is estimated by the Griffith-Irwin relationship [47] for the MgO investigated in this work. This rules out topography as the origin of fracture, because slip steps, the largest "sharp" features on the

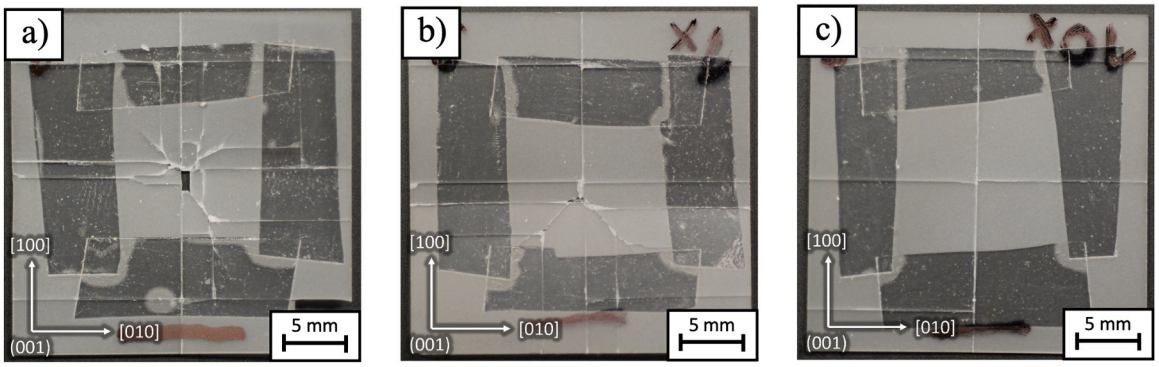

Fig. 9. Typical fracture patterns of specimens from sample BoR−0 in a), BoR−1 in b) and BoR−10 in c). The black regions are pieces of adhesive tape, and felt tip pen markings help with specimen alignment to the fixture. Both were applied to the compression loaded face prior to testing. Felt tip pen lines are parallel to the scratch tracks, if applicable.

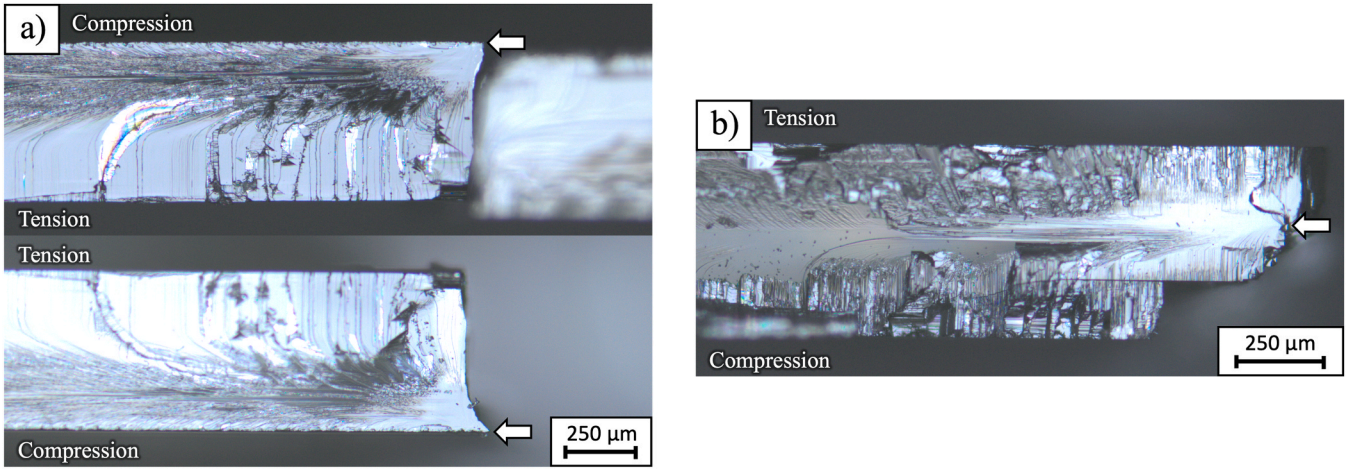

Fig. 10. Invalid types of failure with contact failure shown in a) and bulk failure shown in b). Note that a) does not show the edge of the specimen, but rather the edge of a fragment that was located close to the specimen center. White arrows mark the fracture origins.

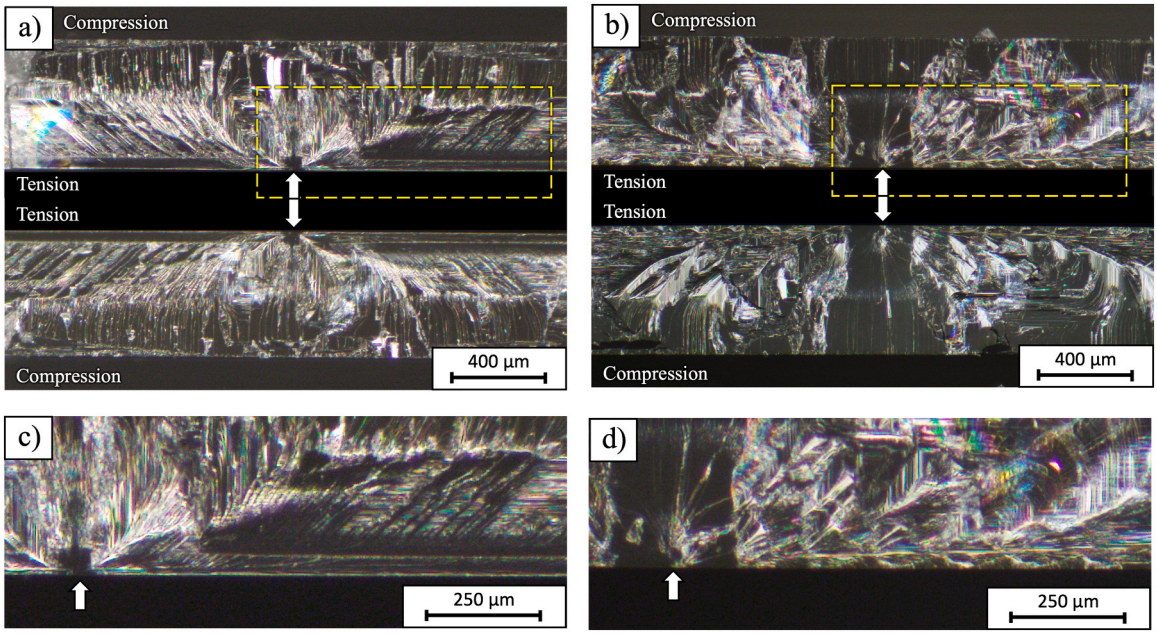

Fig. 11. Two distinctly different types of failure from sample BoR−10 with “parallel failure” shown in a) and “orthogonal failure” shown in b). A detail of a) (marked in yellow) is given in c), and a detail of b) is given in d). Fracture origins are marked by white arrows.

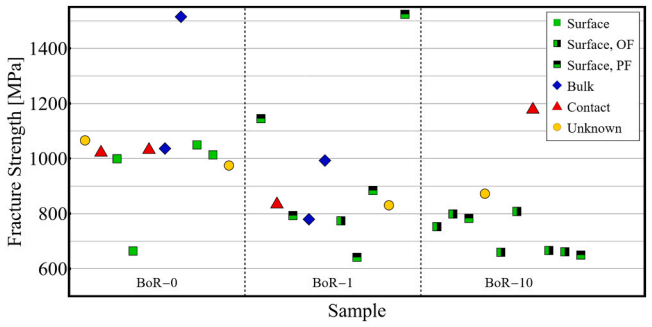

Fig. 12. Individual specimen strength for all samples with color-coded results of fractography.

Table 4
Average strength and standard deviation of specimens before (σ_{mean}) and after censoring ($\sigma_{mean,\ cens}$). After censoring, 4, 6 and 8 specimens were utilized to calculate the mean strength for samples BoR−0, BoR−1 and BoR−10, respectively.

Sample [-]	σ_{mean} [MPa]	$\sigma_{mean,\ cens}$ [MPa]
BoR−0	1037 ± 204	931 ± 179
BoR−1	920 ± 252	960 ± 323
BoR−10	783 ± 159	722 ± 70

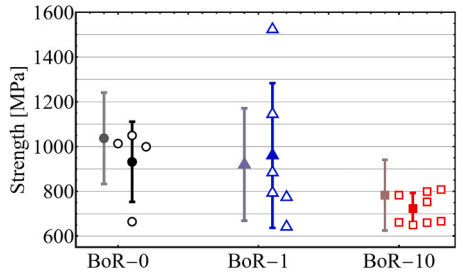

Fig. 13. Average specimen strength of all samples (filled markers) of batch 2 after censoring and respective individual values (open markers). The initial results are shown as grayed markers (left-hand side for each sample).

surface that could act as notches, are only ~10–40 nm in height, as confirmed by vertical scanning interferometer (Bruker Contour GT-X500, Billerica, MA 01821, USA). The scratch tracks themselves are ~100 μm wide, but only 0.3 μm deep with a circular arc profile in cross-section, which renders them malign stress concentrators.

While no cracks through the application of cyclic Brinell scratching have been reported so far [13,25], a certain degree of sub-surface damage is still possible. A very likely form of this damage during indentation experiments in MgO is the creation of immobile dislocation junctions (Lomer locks), which cause pile-up events according to Keh et al. [17,48]. During plastic deformation under an indenter, dislocations from two different active glide planes spontaneously react to form a new dislocation segment on a third, non-active glide plane. Keh et al. showed that this reaction is favourable by lowering the total energy [17]. Additional incoming dislocations from the two original glide planes are blocked by the immobile lock, piling up in front of this obstacle and local stress concentrations beneath the surface are formed [17]. The resulting local stress $\sigma_{pile-up}$ is of tensile character and can be crudely estimated using Eq. (1) given in [49]:

$$\sigma_{pile-up} = \frac{G \bullet N \bullet \|b\|}{\pi \bullet (1-\nu) \bullet L} \tag{1}$$

Here, G is the shear modulus, N is the number of dislocations participating in the pile-up, b is the burgers vector, ν is Poisson's ratio and L is the length of the pile-up. Assuming 100–150 dislocations in the pile-up (based upon a slip step height of ~20 nm, as the burgers vectors need to add up to this height) and a pile-up length of ~1 μm (as was assumed by Hirth and Lothe in [49]), the pile-up stress can easily reach 2 GPa and more. Due to the rough assumptions in this model, which could be refined by extensive transmission electron microscope studies of the pile-ups beyond the scope of this work, the stress could even be several times higher. It is unclear whether this stress already initiates a micro-crack invisible to the characterization methods used here during scratching. When applying the macroscopic bending however, the Lomer locks should be considered as critical defects that might become the origin of fracture.

The concentration of the Lomer locks scales with dislocation density and is also apparent by the hardness increase (i.e. work hardening) that was previously reported [24]. While global surface residual stresses (up to 2 GPa [25]) have been found to be introduced with the used scratching method [25], they are compressive, which should lead to an apparent increase in bending strength, not a decrease as observed. However, in analogy to other surface hardening methods such as shot peening or deep rolling, a smaller region of tensile stress beneath the compressively loaded region is observed, which would further increase the criticality of local sub-surface stress concentrations. As mentioned above, the stress concentrations caused by Lomer-locks might dominate locally over the residual stress, as they are of the same order of magnitude.

Furthermore, different time scales are involved during failure. On one hand, a crack accelerates to the material's speed of sound

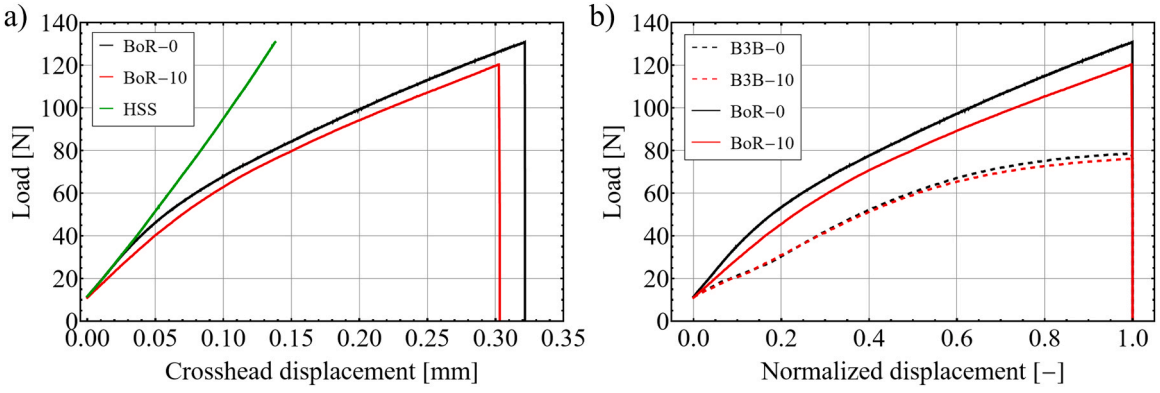

Fig. 14. a) gives the load-displacement curve for two BoR-specimens, with the black line representing a reference specimen (from sample BoR−0) and the red line representing a dislocation-engineered specimen (from sample BoR−10). The green line represents the specimen made from HSS. b) gives the load-displacement curve for both B3B- and BoR-specimens. Note that the displacement is obtained through the crosshead displacement and that it is normalized to the maximum displacement of each curve.

(approximately 5100 m/s for {100} planes in MgO [50]) within the specimen. On the other hand, the dislocation speed is typically in the range of 0.1 μm/s to 1 μm/s [51]. Thus, there could be interaction in the first few ms leading to a short period of stable crack propagation. However, the minimum energy required for crack propagation (crack surface energy 2γ) is in the range of the shielding effect of ~500 perfectly mobile dislocations [24]. Therefore, the time frame in which the crack is still in comparable velocity is not long enough to interact with these dislocations. This is especially true for the specimens in this work, as dislocations are hindered in their mobility due to the ultra-high dislocation densities.

In that regard, this work did not manage to assess the isolated impact of an increased dislocation density on the macroscopic strength, as the influence and damage of the scratching technique on the measured strength cannot be separated from the influence of an increased dislocation density. However, at the time of writing, this technique is the only feasible method to introduce high-density dislocations in a uniform manner on a macroscopic scale at room temperature.

For future work, other stress states, like uniaxial bending, and specimen annealing (to reduce the effect of residual stresses) are of interest. In addition, the impact of other techniques for dislocation introduction at room temperature needs to be investigated as well.

4.2. General findings for strength testing of ultra-high strength plates

In the course of this work, several crucial aspects for accurate and reliable strength testing of high-strength plates emerged, which are briefly discussed in the following points:

1. For high strength specimens, edge failure takes on an increasingly important role. Even though biaxial testing of discs and plates is generally well known for its tolerance against edge failure, batch 1 almost exclusively failed due to flaws at the edges. Ultimately, a considerable enlargement of specimen size, specifically specimen overhang, reduced edge stresses to an acceptable level. Consequently, edge quality can also be improved through alternative manufacturing or machining methods.
2. In this work, it was demonstrated that the occurrence of edge failure could only be proven through fractographic analysis. Therefore, it is essential to ensure suitable conservation of specimen fragments to allow for proper post-mortem analysis. Adhesive tape that is applied to the compression loaded face has proven to be a reliable, cost effective and versatile tool for this purpose. Furthermore, it does not interfere with the accuracy of strength testing itself. While the use of adhesive tapes is considered standard practice in some institutions (and is as such not a novel scientific conclusion), it is often overlooked, which is why the authors wanted to reiterate on this topic here.
3. Within the scope of strength testing of high strength specimens, non-linear effects are especially relevant for thin and flexible specimens. In this context, non-linearity refers to a deviation from the linear relationship between the applied load and the maximum tensile stress. Such non-linear effects occur for significant specimen deformation through changes in leverage, or through a change in load application, as described in [30]. As observed in this work, plastic contact deformation can also cause non-linear behavior. Additionally, membrane stresses (i.e. a radial elongation of the neutral axis in the case of biaxial plate testing) become increasingly relevant. They are not considered through conventional descriptions of stress fields in biaxial strength testing methods, which are based on linear plate theory (Ring-on-Ring test, Ball-on-Ring test, Piston-on-Three-balls test [34,52–55]) or linear FEA (Ball-on-Three-Balls test, Three-Balls-on-Three-Balls test [28,56]). For all these effects, a linear analysis would overestimate the applied stress. Thus, if non-linear effects are not accounted for, the specimen's strength is also overestimated.
4. In the case of strength testing of single crystals, the anisotropic elastic properties must be regarded as well. If isotropic properties (Young's modulus $E = 210$ GPa, Poisson's ratio $\nu = 0.25$) are assumed for specimens of batch 1, the maximum tensile stress in the center increases by 15%. Furthermore, edge stresses are reduced by 20%. Overall, an isotropic analysis would falsely imply a significantly lower risk for edge failures. In the end, this simplification could be detrimental for accurate and reliable strength testing.

These aspects are especially important for a multitude of current and relevant types of brittle specimens, like high-strength glasses (low Young's modulus) and single crystals utilized in the semiconductor industry (high strength, anisotropy of elastic properties).

5. Summary

The impact of dislocations on the structural and functional properties of ceramics at room temperature is of major interest and has been investigated in the past years. In the context of mechanical properties, this was mostly performed on a small scale, which misses the link to bulk or macroscale testing results due to the vast difference in critical flaw populations and testing protocols.

Thus, the impact of an increased dislocation density on the macroscopic biaxial strength of MgO single crystals was investigated in this work. The dislocation density was tailored through an established scratching technique. Two batches of commercially polished MgO plates with different dimensions were investigated. Due to a preference for edge failures within batch 1, the testing procedure was adapted for batch 2. Through this modification of the testing protocol, specimens failed as intended, i.e. within the region of highest dislocation density. A significant decrease in macroscopic strength with an increase in dislocation density was observed, while the fractographic patterns changed as well.

The decrease in strength can be explained through the creation of local stress concentrations. These stress concentrations increase the criticality of pre-existing material flaws and are formed through Lomer locks and subsequent dislocation pile-up during the scratching procedure. Additionally, different time scales are involved for crack propagation and plastic deformation so that the shielding effect of dislocations could not come into play at the macroscale.

CRediT authorship contribution statement

Tanja Lube: Writing – review & editing, Validation, Supervision, Resources. **Oliver Preuß:** Writing – review & editing, Resources, Methodology, Investigation, Formal analysis, Conceptualization. **Xufei Fang:** Writing – review & editing, Supervision, Resources, Methodology, Funding acquisition, Formal analysis. **Maximilian Staudacher:** Writing – review & editing, Writing – original draft, Visualization, Validation, Project administration, Methodology, Investigation, Formal analysis, Conceptualization.

Declaration of Competing Interest

The authors declare that they have no known competing financial interests or personal relationships that could have appeared to influence the work reported in this paper.

Acknowledgement

M. Staudacher gratefully acknowledges support by P. Supancic (Montanuniversität Leoben) for anisotropic Finite Element Analysis and R. Thelen (Karlsruhe Institute of Technology) for the scanning interferometer measurement. O. Preuß and X. Fang thank the funding for fundamental research from the European Research Council (ERC Starting Grant, Project MECERDIS, grant No. 101076167). Views and opinions expressed are, however, those of the authors only and do not

necessarily reflect those of the European Union or the European Research Council (ERC). Neither the European Union nor the granting authority can be held responsible for them. The helpful discussions with Prof. J. Rödel at Technical University of Darmstadt are also acknowledged.

Data availability

Data will be made available on request.

References

[1] R.O. Ritchie, The conflicts between strength and toughness, Nat. Mater. 10 (2011) 817–822.
[2] R.O. Ritchie, X.R. Zheng, Growing designability in structural materials, Nat. Mater. 21 (2022) 968–970.
[3] L. Porz, A.J. Klomp, X. Fang, N. Li, C. Yildirim, C. Detlefs, E. Bruder, M. Höfling, W. Rheinheimer, E.A. Patterson, P. Gao, K. Durst, A. Nakamura, K. Albe, H. Simons, J. Rödel, Dislocation-toughened ceramics, Mater. Horiz. 8 (2021) 1528–1537.
[4] W. Ewald, M. Polanyi, Plastizität und Festigkeit von Steinsalz unter Wasser, Z. FüR. Phys. 28 (1924) 29–50.
[5] J.J. Gilman, W.G. Johnston, Observations of dislocation glide and climb in lithium fluoride crystals, J. Appl. Phys. 27 (1956) 1018–1022.
[6] J.J. Gilman, W.G. Johnston, Dislocations in lithium fluoride crystals, in: F. Seitz, D. Turnbull (Eds.), Solid State Physics, Academic Press, 1962, pp. 147–222.
[7] A.E. Gorum, E.R. Parker, J.A. Pask, Effect of surface conditions on room-temperature ductility of ionic crystals, J. Am. Ceram. Soc. 41 (1958) 161–164.
[8] S.M. Copley, J.A. Pask, Plastic deformation of MgO single crystals up to 1600°C, J. Am. Ceram. Soc. 48 (1965) 139–146.
[9] R.B. Day, R.J. Stokes, Mechanical behavior of magnesium oxide at high temperatures, J. Am. Ceram. Soc. 47 (1964) 493–503.
[10] A. Frisch, C. Okafor, O. Preuß, J. Zhang, K. Matsunaga, A. Nakamura, W. Lu, X. Fang, Room-temperature dislocation plasticity in ceramics: Methods, materials, and mechanisms, J. Am. Ceram. Soc. 108 (2025) e20575.
[11] J. Amodeo, S. Merkel, C. Tromas, P. Carrez, S. Korte-Kerzel, P. Cordier, J. Chevalier, Dislocations and Plastic Deformation in MgO Crystals: A Review, Crystals 8 (2018) 240.
[12] C. Okafor, K. Ding, X. Zhou, K. Durst, J. Rödel, X. Fang, Mechanical tailoring of dislocation densities in SrTiO 3 at room temperature, J. Am. Ceram. Soc. 105 (2022) 2399–2402.
[13] X. Fang, O. Preuß, P. Breckner, J. Zhang, W. Lu, Engineering dislocation-rich plastic zones in ceramics via room-temperature scratching, J. Am. Ceram. Soc. 106 (2023) 4540–4545.
[14] W. Pfeiffer, T. Frey, Strengthening of ceramics by shot peening, J. Eur. Ceram. Soc. 26 (2006) 2639–2645.
[15] H. Gopalan, A. Marshal, M. Hans, D. Primetzhofer, N. Cautaerts, B. Breitbach, B. Völker, C. Kirchlechner, J.M. Schneider, G. Dehm, On the interplay between microstructure, residual stress and fracture toughness of (Hf-Nb-Ta-Zr)C multi-metal carbide hard coatings, Mater. Des. 224 (2022) 111323.
[16] P. Carrez, P. Cordier, B. Devincre, L.P. Kubin, Dislocation reactions and junctions in MgO, Mater. Sci.Eng. A 400-401 (2005) 325–328.
[17] A.S. Keh, Cracks due to the piling-up of dislocations on two intersecting slip planes in MgO crystals, Acta Metall. 7 (1959) 694–696.
[18] R. Thomson, Physics of fracture, in: F. Seitz, D. Turnbull (Eds.), Solid State Physics, Academic Press, 1962, pp. 1–129.
[19] K. Higashida, N. Narita, S. Asano, R. Onodera, Dislocation emission from a crack tip in MgO thin crystals, Mater. Sci. Eng. A 285 (2000) 111–121.
[20] J.R. Rice, R. Thomson, Ductile versus brittle behaviour of crystals, Philos. Mag. A J. Theor. Exp. Appl. Phys. 29 (1974) 73–97.
[21] L.L. Fischer, G.E. Beltz, The effect of crack blunting on the competition between dislocation nucleation and cleavage, J. Mech. Phys. Solids 49 (2001) 635–654.
[22] R. Danzer, A general strength distribution function for brittle materials, J. Eur. Ceram. Soc. 10 (1992) 461–472.
[23] A.D.S. Jayatilaka, K. Trustrum, Statistical approach to brittle fracture, J. Mater. Sci. 12 (1977) 1426–1430.
[24] O. Preuß, E. Bruder, J. Zhang, W. Lu, J. Rödel, X. Fang, Damage-tolerant oxides by imprint of an ultra-high dislocation density, J. Eur. Ceram. Soc. 45 (2025) 116969.
[25] O. Preuß, Z. Li, E. Bruder, P. Carrez, Y. Cui, J. Rödel, X. Fang, Stable crack propagation in dislocation-engineered oxide visualized by double cleavage drilled compression test, J. Eur. Ceram. Soc. 46 (2026) 117905.
[26] S. Zaefferer, N.-N. Elhami, Theory and application of electron channelling contrast imaging under controlled diffraction conditions, Acta Mater. 75 (2014) 20–50.
[27] M. Staudacher, T. Lube, J. Schlacher, P. Supancic, Comparison of biaxial strength measured with the Ball-on-Three-Balls- and the Ring-on-Ring-test, Open. Ceram. 6 (2021) 100101.
[28] A. Börger, P. Supancic, R. Danzer, The ball on three balls test for strength testing of brittle discs: stress distribution in the disc, J. Eur. Ceram. Soc. 22 (2002) 1425–1436.
[29] R. Danzer, P. Supancic, W. Harrer, Der 4-Kugelversuch zur Ermittlung der biaxialen Biegefestigkeit spröder Werkstoffe, Tech. Keram. Werkst. (2009) 1–48.
[30] M. Staudacher, T. Lube, P. Supancic, The Ball-on-Three-Balls strength test for discs and plates: Extending and simplifying stress evaluation, J. Eur. Ceram. Soc. 43 (2023) 648–660.
[31] R. Morrell, Biaxial flexural strength testing of ceramic materials, Teddington (2007).
[32] D.K. Shetty, A.R. Rosenfield, P. McGuire, G.K. Bansal, W.H. Duckworth, Biaxial flexure tests for ceramics, Am. Ceram. Soc. Bull. 59 (12) (1980) 1193–1197.
[33] G. de With, H.H.M. Wagemans, Ball-on-Ring test revisited, J. Am. Ceram. Soc. 72 (1989) 1538–1541.
[34] M. Staudacher, P. Supancic, T. Lube, The Ball-on-Ring-test: enhancing an analytical solution by numerical analysis for elastic deformation and small displacements, J. Eur. Ceram. Soc. 43 (2023) 7167–7177.
[35] ISO 20501:2019, Fine ceramics (Advanced Ceramics, Advanced Technical Ceramics) — Weibull Statistics for Strength Data, International Organization for Standardization, Geneva, Switzerland, 2019.
[36] D. Isaak, O. Anderson, T. Goto, Measured elastic moduli of single-crystal MgO up to 1800 K, Phys. Chem. Miner. 16 (1989) 704–713.
[37] M. Staudacher, A. Eggel, P. Supancic, T. Lube, The Ball-on-Three-Balls strength test: effective volumes and surfaces for Weibull strength scaling, J. Eur. Ceram. Soc. 44 (2024) 173–183.
[38] Heinrich Hertz, Über die Berührung fester elastischer Körper, J. FüR. die reine und Angew. Math. 92 (1882) 156–171.
[39] M. Deluca, R. Bermejo, M. Pletz, P. Supancic, R. Danzer, Strength and fracture analysis of silicon-based components for embedding, J. Eur. Ceram. Soc. 31 (2011) 549–558.
[40] M. Gruber, I. Kraleva, P. Supancic, J. Bielen, D. Kiener, R. Bermejo, Strength distribution and fracture analyses of LiNbO 3 and LiTaO 3 single crystals under biaxial loading, J. Eur. Ceram. Soc. 37 (2017) 4397–4406.
[41] M. Gruber, A. Leitner, D. Kiener, P. Supancic, R. Bermejo, Effect of crystal orientation on the hardness and strength of piezoelectric LiNbO3 substrates for microelectronic applications, Mater. Des. 213 (2022) 110306.
[42] M. Gruber, A. Leitner, I. Kraleva, D. Kiener, P. Supancic, R. Bermejo, Understanding the effect of surface flaws on the strength distribution of brittle single crystals, J. Am. Ceram. Soc. 101 (2018) 5705–5716.
[43] A.A. Wereszczak, A.S. Barnes, K. Breder, S. Binapal, Probabilistic strength of {1 1 1} n-type silicon, J. Mater. Sci. Mater. Electron. 11 (2000) 291–303.
[44] K. Yasuda, S.-D. Kim, Y. Kanemichi, Y. Matsuo, S. Kimura, Influence of grain size and temperature on fracture toughness of MgO sintered body, J. Ceram. Soc. Jpn. 98 (1990) 1103–1108.
[45] D.A. Shockey, G.W. Groves, Effect of water on toughness of MgO crystals, J. Am. Ceram. Soc. 51 (1968) 299–303.
[46] P. Lazar, M. Otyepka, Accurate surface energies from first principles, Phys. Rev. B 91 (2015) 115402.
[47] D. Munz. Ceramics: Mechanical Properties, Failure Behaviour, Materials Selection, first ed., Springer, Berlin, Heidelberg, 1999 (Berlin / Heidelberg).
[48] P. Carrez, P. Cordier, B. Devincre, L.P. Kubin, Dislocation reactions and junctions in MgO, Materials Science Engineering A 400-401 (2005) 325–328.
[49] P.M. Anderson, J.P. Hirth, J. Lothe, Theory of Dislocations, Cambridge University Press, New York, NY, USA, 2017.
[50] F.P. Bowden, J.H. Brunton, J.E. Field, A.D. Heyes, Controlled fracture of brittle solids and interruption of electrical current, Nature 216 (1967) 38–42.
[51] U. Messerschmidt. Dislocation Dynamics During Plastic Deformation, first ed., Springer, Berlin, Heidelberg, 2010 (Berlin / Heidelberg).
[52] ASTM C 1499-05, Test Method for Monotonic Equibiaxial Flexural Strength of Advanced Ceramics at Ambient Temperature, ASTM International, West Conshohocken, PA, 2005.
[53] A.F. Kirstein, R.M. Woolley, Symmetrical bending of thin circular elastic plates on equally spaced point supports, J. Res. Natl. Bur. Stand. Sect. C Eng. Instrum. 71C (1967) 1.
[54] J.B. Wachtmann Jr, W. Capps, J. Mandel, Biaxial flexure tests of ceramic substrates, J. Mater. (1972) 188–194.
[55] S.P. Timoshenko, S. Woinowsky-Krieger. Theory of Plates and Shells, second ed., McGraw-Hill, New York, 1987.
[56] T. Fett, G. Rizzi, E. Ernst, R. Müller, R. Oberacker, A 3-balls-on-3-balls strength test for ceramic disks, J. Eur. Ceram. Soc. 27 (2007) 1–12.